PHYSICAL REVIEW FLUIDS **6**, 044002 (2021)

Editors' Suggestion

Thin film instability driven dimple mode of air film failure during drop impact on smooth surfaces

Lige Zhang, Tejaswi Soori, Arif Rokoni, Allison Kaminski, and Ying Sun[*]
Department of Mechanical Engineering and Mechanics, Drexel University, Philadelphia, Pennsylvania 19104, USA

(Received 28 August 2020; accepted 23 March 2021; published 12 April 2021)

Air film stability underneath a drop is crucial for drop contact dynamics upon impact. An unstable film leads to the drop contacting the surface and subsequent spreading or splashing. Apart from previously reported film and kink contact modes, here we present the experimental evidence for a dimple failure mode of an air film, driven by a thin film instability when a drop impacts onto an atomically smooth surface. The dimple failure occurs beyond the inertial-capillary timescale and is initiated when the dimple inverts at the drop's central axis. For the same impact Weber number, the dimple failure observed in low-viscosity drops is absent at a higher viscosity, due to damping of capillary waves.

DOI: 10.1103/PhysRevFluids.6.044002

I. INTRODUCTION

When a liquid drop impinges onto a smooth, dry surface, a thin layer of air evolves between the drop and the surface [1,2]. Depending on the Weber number, $\mathrm{We} = \rho_l U_0^2 R/\gamma$, where ρ_l is the liquid density, U_0 the impact velocity, R the drop radius, and γ the liquid surface tension, the drop can either bounce [3–5] or contact the surface, eventually leading to spreading [6,7] and splashing [8–10]. Past studies on drops impacting dry, smooth surfaces have reported two key modes of contact: (a) the film mode [11] (or the first kink mode [12–14]) and (b) the kink mode [11] (or the second kink mode [12]) at the kink of the air film right outside the dimple and at the maximum extension of the drop, respectively [11–14]. For a water drop impacting a dry surface at 1 atm, with increasing We, one can observe a transition from drop bouncing ($\mathrm{We} \ll 1$) to the kink mode ($\mathrm{We} \approx 1$), and eventually the film mode ($\mathrm{We} \gg 1$) of contact as shown in Fig. 2(a). Recently, a third contact mode called the dimple mode was also reported for a drop impacting on a smooth surface [11,15], where the contact is initiated at the drop's central axis. This new contact mode occurs when the dimple, formed underneath the drop due to a pressure buildup within the air layer [12,16–18], crashes downward owing to impact-induced capillary waves. However, the detailed mechanism of the dimple mode and its experimental evidence prior to the contact are still lacking.

Prior to drop contact with a surface, impacts above a threshold $\mathrm{We} \approx 4$ generate capillary waves that propagate along the surface to the apex of the drop, exhibiting the characteristic pyramid shapes, eventually creating an air cavity at the drop center [19,20]. The capillary wave occurs when its wavelength $\lambda_c = \gamma/\rho_l U_0^2$ is smaller than the drop radius R while its attenuation length $l \sim \sqrt{\frac{9}{128\pi^3}\frac{\gamma^2}{\rho_l U_0^3 \mu_l}}$ [21] is larger than R, where μ_l is the drop viscosity. Increase in the drop viscosity leads to an exponential decay of the capillary wave's local amplitude $a(x) = a_0 e^{-\alpha x}$ due to viscous dissipation, where a_0 is the initial amplitude at $x = 0$ and $\alpha = \mu_l\sqrt{\frac{128\pi^2}{9\rho_l\gamma\lambda_c^3}}$ is the attenuation

---

[*] ys347@drexel.edu

2469-990X/2021/6(4)/044002(11)

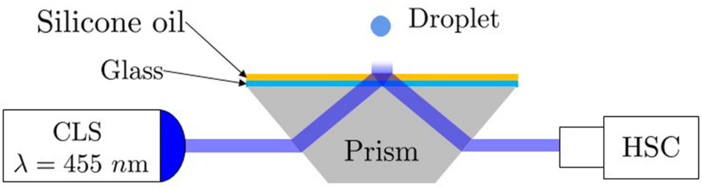

FIG. 1. A schematic of the high-speed total internal reflection microscopy imaging setup used in our drop impact study. An optically transparent lubricated substrate is placed on top of a dove prism and is illuminated by a collimated light source (CLS) of 455-nm wavelength. A high-speed camera (HSC) captures the TIRM images.

coefficient. Moreover, during drop impact on dry surfaces, the closure of air cavity leads to either bubble entrapment within the drop or bubble attachment to the substrate, depending on the cavity depth [19,20,22]. However, the effects of capillary waves and air cavity on the air film failure mechanics, more precisely on the dimple mode, have remained largely unexplored. What effect does the downward moving air cavity have on the dynamics of the dimple underneath it?

In this study, we present the theory and experimental evidence of an air film failure mode where the dimple collapses due to thin film instability driven by a combined effect of capillary wave and air cavity, leading to air film rupture at the drop's central axis. The interstitial air film underneath an aqueous drop impacting a lubricated smooth surface is visualized using the total internal reflection microscopy (TIRM) which can probe the air film of thickness $\sim\mathcal{O}(10^0 - 10^2)$nm [4,15,23]. The drop viscosity and impact We are varied to study the effects of viscous damping of capillary wave and air cavity on the air film dynamics and subsequent drop-surface contact mechanisms. While low-viscosity drops either bounce or exhibit dimple collapse or film contact mode, higher-viscosity drops exhibit only bouncing and the film mode of contact. From both experiments and theory, we show that the capillary waves and air cavity are precursors to the thin film instability driven dimple failure mode. Our motivation for studying drop impact on a lubricated surface, as a perfect case for an atomically smooth surface [15,24], is due to its ability in isolating the effects of surface asperities that cause a sudden rupture of the air film [5,12,13,25].

II. EXPERIMENTS

Figure 1 shows the schematic of the TIRM imaging setup used in our droplet impact experiments. Deionized (DI) water, 40 wt% glycerol, and 60 wt% glycerol aqueous solutions were used to study the effect of liquid viscosity. Silicone oil of viscosity 10^5 cSt was spin coated onto a glass slide at a rotational speed of 10 000 rpm for 25 min to prepare the lubricated surface, and the film provided an optically transparent pathway for the TIRM measurement. The silicone oil film thickness was measured by taking weight difference before and after spin coating and was 5 μm, resulting in a dimensionless film thickness $\delta = h_{\text{oil}}/2R = 0.005 \ll 0.7$ [26], the threshold for negligible lubricant deformation below which the bottom glass substrate imposes geometric restrictions that cause reduced energy transfer from the impacting droplet to the liquid film [24]. In our previous study [15], we investigated the effect of viscosity of the lubricating silicone oil film on the oil film deformation during droplet impact and found that for a 5 μm thick film of viscosity 5 cSt, the surface waves were overdamped within $\mathcal{O}(10\ \mu\text{m})$, an order of magnitude smaller than the initial dimple radius of 250 μm, thereby confirming that the film deformation did not have significant contribution to the air film dynamics. The refractive index of glass and dove prism was $n = 1.52$. The lubricated substrate was placed on top of a dove prism and a p-polarized chromatic light source at a wavelength of $\lambda = 455$ nm was used to illuminate the top of the silicone oil-air interface at an incident angle of 49.9°. A Phantom V711 high-speed camera captured the TIRM images at a pixel resolution of 13 μm and a frame rate of 50 000 frames per second, which corresponds to a temporal resolution of 20 μs. The high-speed TIRM images were output and stored in 16-bits grayscale images for

TABLE I. Physical properties of fluids at 25 °C in our experiments.

Fluids	Density, ρ_l (kg m^{-3})	Viscosity, μ_l (cP)	Surface tension to air, γ (Nm^{-1})	Refractive index, n
DI water	997	1	0.072	1.33
40 wt% glycerol aqueous solution [27]	1097	3.7	0.07	1.38
60 wt% glycerol aqueous solution [27]	1151	10.7	0.068	1.41
Silicone oil [28]	977	97.7×10^3	0.021	1.40

analysis. The TIRM measurement was calibrated against Shirota *et al.*'s correction [23] and was used to extract air film height, h. Drop radius R and impact velocity U_0 were measured using side-view images. Drop radius was maintained at $0.64 \leqslant R \leqslant 1.10$ mm and the impact velocity $(0.3 \leqslant U_0 \leqslant 0.9)$ m/s was altered by changing the drop dispensing height. Properties of fluids used in our experiments are tabulated in Table I.

Figure 2(b) shows the schematic of the drop dynamics during the impact process at We ≈ 4. Here, $t = 0$ corresponds to the time instance when the drop appears within the evanescent field of the TIRM image. The capillary wave is excited from the drop bottom edge and propagates over the drop surface towards the apex during $0 < t < \tau$ [$\tau \equiv \sqrt{(\rho_l R^3/\gamma)}$ the inertial-capillary timescale], while generating characteristic pyramid shapes [19] whose wavelength is λ_c. When $t \approx \tau$, the convergence of the capillary wave at the apex creates an air cavity at the drop center whose depth varies both with U_0 and μ_l. The higher the μ_l, the smaller the depth, due to viscous damping.

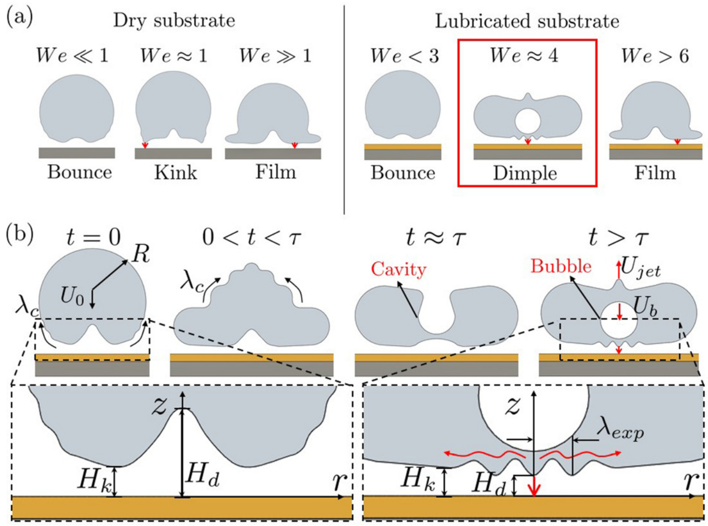

FIG. 2. (a) Schematics of contact modes for water drop impacting on dry and lubricated substrates [4,14,29], where the red arrows indicate the contact locations. The red-bordered panel corresponds to the dimple mode of the current study at We ≈ 4. (b) Schematics of drop evolution undergoing dimple collapse at four different instances with respect to the inertial-capillary timescale, $\tau \equiv \sqrt{(\rho_l R^3/\gamma)}$. The spherical drop of radius, R, impacting at a velocity, U_0, deforms and creates an air film at $t = 0$. The maximum and minimum air film heights are at the center of the air dimple, H_d, and at maximum curvature kink, H_k, respectively, for $t \leqslant \tau$. Capillary wave of wavelength, λ_c, propagates along the drop surface during $t \leqslant \tau$. A representative wavelength, λ_{exp}, is the distance between two consecutive local minima in an air film profile at $t > \tau$, shown in (b). z and r are the axial and radial coordinates, respectively.

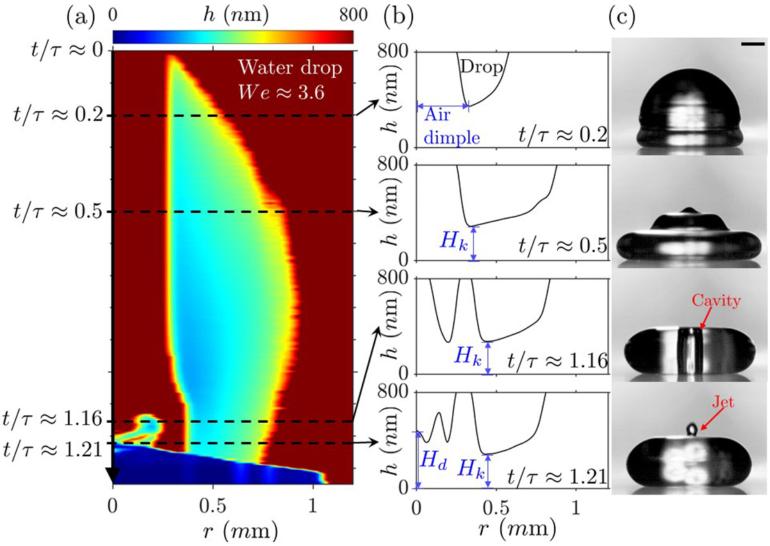

FIG. 3. (a) Kymograph of air film height for a water drop at We ≈ 3.6, where r is the radial position of the air film, the vertical axis is the dimensionless time t/τ, and the color indicates the air film height, h, measured from TIRM images. The air film profiles in (b) correspond to the dashed lines at $t/\tau \approx 0.2$, 0.5, 1.16, and 1.21, shown in (a), respectively. (c) Synchronized side-view images at the four dimensionless times. Scale bar in (c) is 0.5 mm.

At $t > \tau$, the cavity suddenly closes at the top, creating the well-known singular jet ejection [20] and bubble entrapment [19,20,22]. Prior to the air cavity closure, the apex of the drop travels downward, eventually inverting the top-facing dimple. Due to a sudden increase in air pressure inside the dimple region, an outward air flow is set up creating a shear flow at the drop-air interface (see Fig. 7 and related discussion for details), causing interfacial perturbations at the drop bottom with wavelength λ_{exp}. The key geometric parameters pertaining to the air film are the dimple height, H_d, located at the central axis of the drop, and the kink height, H_k, located at the drop interface with the highest local curvature, where the latter is associated with the film mode of contact.

III. RESULTS AND DISCUSSION

Figure 3(a) shows a kymograph of the air film profile for a water drop at We ≈ 3.6, where the x axis is the radial position r of the air film, the y axis is the dimensionless time t/τ, and the colors indicate the air film height h, measured from TIRM images. The four dashed lines in Fig. 3(a) indicate the times at $t/\tau \approx 0.20$, 0.50, 1.16, and 1.21, where the air film profiles and drop shapes of the corresponding instances are shown in Figs. 3(b) and 3(c), respectively. The blue arrows in Fig. 3(b) indicate the locations of characteristic air film geometry: dimple (H_d) and first kink (H_k), while the red arrows in Fig. 3(c) show the cavity and the ejected jet. The minimum air film height reduced due to thin film drainage until $t/\tau \to 1$, beyond which the air film morphology exhibited perturbations. While for $t/\tau < 1$ the minimum air film thickness was located at the first kink H_k, as $t/\tau \to 1$, multiple local minima appeared within the dimple region of the air film due to perturbations. At $t/\tau > 1$, the thin film instability wave in the air film became prominent, shown in the bottom inset of Fig. 3(b), and the instability wavelength, λ_{exp}, was measured by taking average distance between different minima locations of the air film. These thin film perturbations of the drop-air interface finally led to a sudden decrease in the dimple height H_d, ultimately leading to the air film rupture at the drop center at $t/\tau \approx 1.24$.

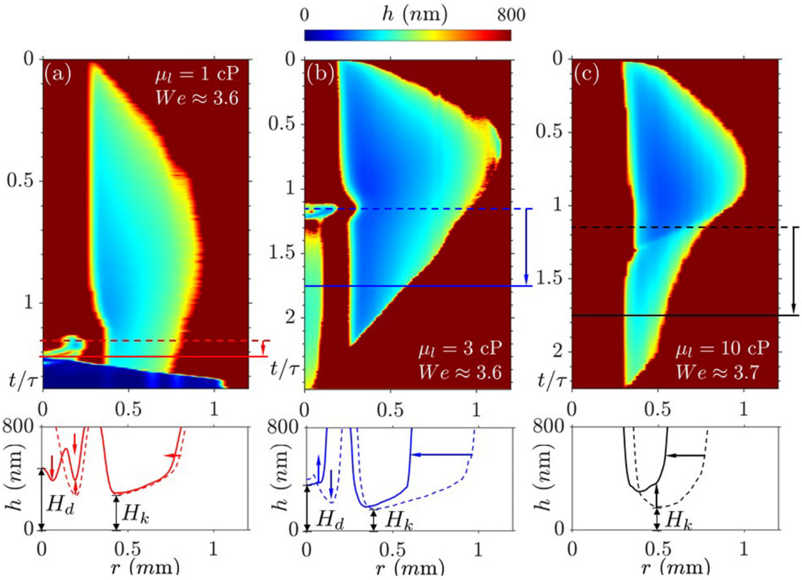

FIG. 4. Kymograph of the air film height vs dimensionless time t/τ for (a) a water drop, $\mu_l = 1$ cP, We $\approx$ 3.6, and aqueous glycerol drops (b) $\mu_l = 3$ cP, We $\approx$ 3.6, and (c) $\mu_l = 10$ cP, We $\approx$ 3.7, respectively. Dashed and solid lines in the kymographs correspond to the 2D air film profiles shown directly below them, which compare the undamped and damped air film perturbations when increasing the drop viscosity. See the air film evolution video in the Supplemental Material [30].

To study the failure mechanism due to air film instability, drops of various viscosities but similar impact We were created. In Fig. 4, we show kymograph comparison of the air profiles between three drops: (a) water ($\mu_l = 1$ cP), (b) 40 wt% glycerol ($\mu_l = 3$ cP), and (c) 60 wt% glycerol ($\mu_l = 10$ cP) aqueous solutions, respectively. The dashed and solid lines in the kymographs correspond to the instances of 2D air film profiles shown in the insets directly below them. As seen in Figs. 4(a) and 4(b), the air film exhibited thin film instabilities for time $t > \tau$, while in Fig. 4(c) the perturbations were completely absent, confirming that the increase in droplet viscosity suppresses thin film perturbations. During $0 < t < \tau$, the air film extended radially outwards for all three drops. However, the final fates of the drops were different due to the differences in air film behaviors at $t/\tau > 1$. As seen in kymographs of water and 3 cP drops, the perturbations occurred at similar time instances, $t/\tau \approx 1.16$. While the perturbations grew in the case of a water drop, finally resulting in a drop-surface contact due to the dimple mode, the perturbations for the 3 cP drop decayed and the drop radially retracted and eventually bounced off. As the drop viscosity increased to 10 cP, no perturbations were seen throughout the air film evolution and the drop eventually bounced off. Instead of exhibiting a dimple failure, 3 and 10 cP drops skated on the air film for a period of more than 2τ [19] and bounced off. Given that both water and a 3 cP drop exhibited air film perturbations, but only the water drop failed via the dimple mode, what dictates their final fate?

When the drop-air interface approaches the substrate, only surface tension and vdW forces act on the air film in the form of capillary and disjoining pressures, respectively. Based on the thin film stability analysis [11], a perturbed air film becomes unstable when its wavelength is greater than the critical wavelength of the fastest growing wave, $\lambda_{\max}^{\text{crit}} = H_{\min}^2\sqrt{(\frac{16\pi^3\gamma}{A_{132}})}$, where $A_{132} = 4.76 \times 10^{-20} J$ is the Hamaker constant [31]. In Ref. [11], the authors reported that the numerically measured growth rate of the fastest growing mode agreed well with their theoretical predictions. When the perturbation wavelength is smaller than the critical wavelength $\lambda_{\max}^{\text{crit}}$, the film stabilizes due to surface tension dominating the van der Waals (vdW) interactions. However, for a

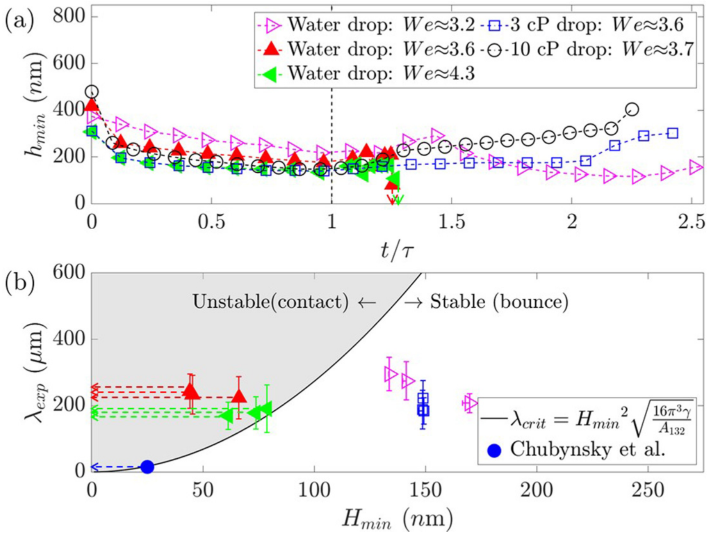

FIG. 5. (a) The instantaneous minimum air film height, $h_{\min}$, vs the dimensionless time, t/τ, for water drops and aqueous glycerol drops at the viscosity of 3 and 10 cP. The location within the air film where $h_{\min}$ is measured temporally fluctuates between the dimple and kink, during the air film evolution. (b) Measured air film wavelength, λ_{exp}, vs the absolute minimum air film height, $H_{\min}$, together with the critical air film wavelength, $\lambda_{\max}^{\mathrm{crit}}$, predicted by the thin film stability theory [11]. Each color symbol in (b) represents one drop impact event for a specific liquid viscosity and We shown in (a). Closed symbols represent air films undergoing dimple failure due to instability and open symbols represent stable air films. Dashed arrows indicate rapid air film collapse at a height of $H_{\min}$. The minimum film height $H_{\min}$ in (b) is the absolute minimum film height obtained from (a). Solid blue circle corresponds to the film mode result reported in Ref. [11] with unstable wavelength $\lambda_{\mathrm{num}} = 10\ \mu$m at $H_{\min} = 25$ nm. Vertical error bars in (b) represent the standard deviation in measured λ_{exp} while the one-sided horizontal error bars for bouncing drops account for the limitations in temporal resolution of the TIRM imaging.

perturbation wavelength larger than the critical wavelength, vdW interactions are strong enough to initiate a drop-surface contact due to disjoining pressure dominating the capillary pressure.

Figure 5(a) shows the instantaneous minimum air film height $h_{\min}$ versus t/τ for water drops at We $\approx$ 3.2, 3.6, and 4.3, and for 3 and 10 cP aqueous glycerol drops at We $\approx$ 3.6 and 3.7, respectively. While all drops exhibit similar air film drainage behaviors for times $t/\tau < 1$, water drop at the lowest We as well as 3 and 10 cP aqueous glycerol drops, represented by open markers, exhibit skating between $1 \leqslant t/\tau \leqslant 2$ and ultimately bounce off. However, for time $t/\tau > 1$, water drops at We $\approx$ 3.6 and 4.3, represented by closed markers, contact the substrate via dimple collapse due to thin film instability. Figure 5(b) shows the experimentally measured perturbation wavelengths, λ_{exp}, versus the absolute minimum air film height before contact/bouncing, $H_{\min}$, for the drop impact cases shown in Fig. 5(a) in comparison with the critical wavelength, $\lambda_{\max}^{\mathrm{crit}}$ [11]. In Fig. 5(b), the value $H_{\min}$ corresponds to the minimum air film height immediately prior to bouncing and contact, for stable and unstable drops, respectively. For stable drops, this corresponds to when an increase in $h_{\min}$ is observed, and for unstable drops, the last TIRM frame prior to contact. Stable drops that exhibit bouncing have experimentally measured perturbation wavelengths (open symbols) less than the critical wavelength (solid line), $\lambda_{\mathrm{exp}} < \lambda_{\max}^{\mathrm{crit}}$, and unstable drops that exhibit dimple mode of contact have experimentally measured perturbation wavelength (closed symbols), $\lambda_{\mathrm{exp}} > \lambda_{\max}^{\mathrm{crit}}$. As the air film of the 10 cP drop does not experience any perturbation, the air film wavelength is not measurable in this case. Vertical error bars in Fig. 5(b) represent the standard deviation in λ_{exp}. It is important to note that, although increasing temporal resolution of TIRM imaging leads to $H_{\min} \rightarrow 0$ for unstable drops, it does not affect the experimentally observed instability wavelength, λ_{exp}, which

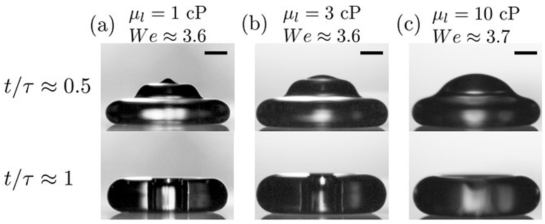

FIG. 6. Side-view images at the instances of $t/\tau \approx 0.5$ and $t/\tau \approx 1$ for (a) a water drop, $\mu_l = 1$ cP, We $\approx$ 3.6, and aqueous glycerol drops (b) $\mu_l = 3$ cP, We ≈ 3.6, and (c) $\mu_l = 10$ cP, We ≈ 3.7, respectively. Scale bar is 0.5 mm. See the drop shape evolution video in the Supplementary Material [30].

is always larger than the critical wavelength, $\lambda_{\max}^{\text{crit}}$. The one-sided horizontal error bars for bouncing drops in Fig. 5(b) account for the limitations in temporal resolution of the TIRM imaging, calculated based on simple equations of motion, resulting in minimum air film heights less than 1 nm below the measured $H_{\min}$ values.

Chubynsky *et al.* [11] investigated the film and kink modes of contact for drop impact on dry, smooth surfaces using numerical simulations and thin film stability theory. For the film contact mode, an air film of height $H_{\min} = 25$ nm leads to a numerically simulated critical wavelength of $\lambda_{\text{num}} \approx 10$ μm, compared to the theory-predicted value of $\lambda_{\max}^{\text{crit}} = 15$ μm [11]. However, experimental wavelength measurement of thin film instabilities for film and kink modes is difficult using our current imaging resolution.

In order to study the effect of drop viscosity on the capillary wave driven drop deformation and the subsequent air cavity formation, in Fig. 6 we show side-view images of water and aqueous glycerol drops with different viscosities at the instances of $t/\tau \approx 0.5$ and $t/\tau \approx 1$, where the drop impact events correspond to the cases shown in Fig. 4. The capillary wave is propagated along the surface to the apex of the drop during $t/\tau < 1$. For the water drop (We ≈ 3.6, $R = 1$ mm, $U_0 = 0.51$ m/s) shown in Fig. 6(a) and 3 cP aqueous glycerol drop (We ≈ 3.6, $R = 0.98$ mm, $U_0 = 0.48$ m/s) shown in Fig. 6(b), the measured wavelengths were $\lambda_c \approx 430$ and ≈ 400 μm, respectively. As the viscosity increased to 10 cP, the wavelength was not measurable due to the absence of pyramidal structures. The cavity depth of the 10 cP drop at the instance $t/\tau \approx 1$ was much smaller compared to water and 3 cP drops. This was due to the exponential decay of the capillary wave with the attenuation coefficient, $\alpha = \mu_l\sqrt{128\pi^2/9\rho_l\gamma\lambda_c^3}$ [21]. Therefore, the air film perturbation was suppressed for drop viscosity greater than 10 cP, and the stabilized air film led to the drop bounce off. The capillary waves over the droplet top surface and at the unstable air film observed here should not be confused with those seen during postcontact air disk retractions [32–34].

To support our hypothesis of the cavity-driven dimple inversion and the subsequent shear flow conditions at the drop-air interface due to an outward air flow during the air film drainage, the air film is divided into dimple, film, and edge regions. A combined Poiseuille and Couette flow condition was recently proposed [24] to study air film drainage during drop impact on liquid films and showed that a slip velocity at the interfaces leads to a faster air film drainage and the subsequent failure. In the current study, the air layer is assumed to be incompressible with Navier slip conditions at the drop-air and air-oil interfaces [15,24], and the air layer velocity profile is assumed similar to those presented in Refs. [11,24], as depicted in Fig. 7(a). Figure 7(b) shows the experimentally determined transient air film profile in the dimple, film, and edge regions beyond the inertial-capillary timescale, which corresponds to the drop impact case shown in Fig. 3. The color scheme represents the dimensionless time t/τ. The control volumes of the dimple ($V_{1,0}: r \in [0, 0.4]$ mm), film ($V_{2,0}: r \in [0.4, 0.8]$ mm), and edge ($V_{3,0}: r \in [0.8, 1.2]$ mm) regions are 900 nm thick, which is the TIRM measurement limit. The instantaneous volumes of dimple, film, and edge regions are $V_1(t)$, $V_2(t)$, and $V_3(t)$, respectively. Figure 7(c) shows the dimensionless instantaneous air film volume, $V_i/V_{i,0}$, as a function of dimensionless time t/τ for each region. From Fig. 7(c), we notice a sudden reduction in dimple region volume at $t/\tau > 1.13$, which coincides with the air cavity's downward propagation

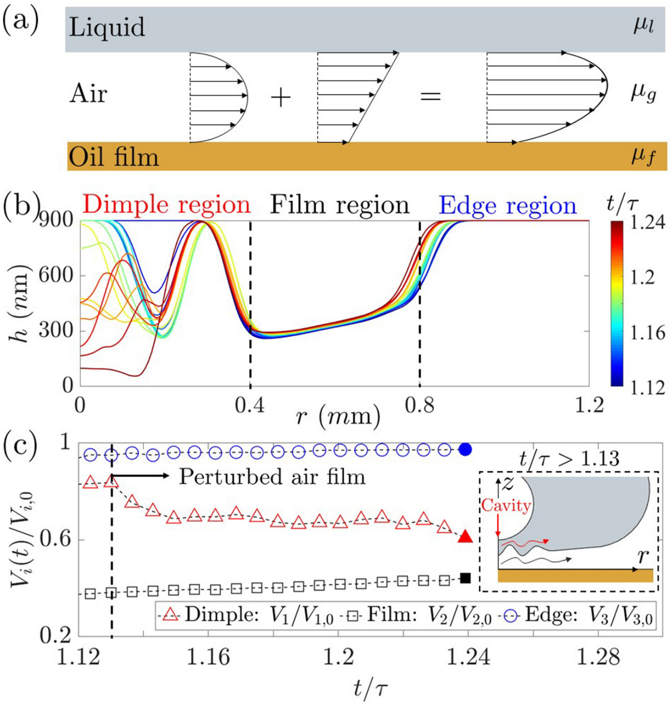

FIG. 7. (a) Schematics of the velocity profile inside the air film. (b) Transient air film profile in the sectioned control volumes before a dimple mode contact for a water drop at We ≈ 3.6, the conditions considered in Fig. 3. The color scheme represents the dimensionless time t/τ. The control volumes are 900 nm thick and sectioned into dimple ($V_{1,0} : r \in [0, 0.4]$ mm), film ($V_{2,0} : r \in [0.4, 0.8]$ mm), and edge ($V_{3,0} : r \in [0.8, 1.2]$ mm) regions. The instantaneous volumes of these three regions are $V_1(t)$, $V_2(t)$, and $V_3(t)$, respectively. (c) Dimensionless instantaneous air film volume, $V_i/V_{i,0}$, vs t/τ in the dimple, film, and edge regions. The solid symbols represent the timeframe right before the dimple contact. The inset schematic of (c) corresponds to a perturbed air film at $t/\tau > 1.13$, where the black and red arrows show the direction of air and liquid motion, respectively.

time as shown in Fig. 3. This observation confirms the enhanced air film drainage in the dimple region due to cavity formation and subsequent dimple inversion. The reduction of the air volume underneath the dimple region does not cause a significant change in the air volume underneath the film and edge regions due to the air film perturbations exhibiting highly transient phenomena.

Under ambient conditions, the mean-free path of air $L \approx 70$ nm results in a Knudsen number $\mathrm{Kn} = L/H_d$ of $\mathcal{O}(10^{-2})$ prior to instability, appropriate for the Navier-slip assumption at both the drop-air and air-oil film interfaces. Here, $H_d \sim RSt^{-2/3}$ [35] is the dimple height and $St = \rho_l R U_0/\mu_g$ is the Stokes number, where μ_g is the gas viscosity. Within the dimple region of the air film, the gas pressure P_g is balanced by the liquid capillary pressure $P_{\gamma,\mathrm{dimp}}$, the inertial pressure P_I, and the disjoining pressure P_d, which follows $P_g \sim P_{\gamma,\mathrm{dimp}} + P_I + P_d$. The capillary pressure is $P_{\gamma,\mathrm{dimp}} \sim \gamma/R$ and the inertial pressure is $P_I \sim \rho_l U_0^2 R/L_0$ [16], where $L_0 \sim \sqrt{R\,H_d}$ is the radial extent of the dimple. For a water drop ($R = 1$ mm, $U_0 = 0.51$ m/s) undergoing a dimple mode of contact (see Fig. 3), the radial extent of the dimple $L_0 = 0.5$ mm is measured at $t = 0$ when the air film starts to appear in the TIRM image. Therefore, the capillary and inertial pressures are $P_{\gamma,\mathrm{dimp}} \sim \mathcal{O}(10^1)$ Pa and $P_I \sim \mathcal{O}(10^2)$ Pa, respectively. Before the droplet-air interface exhibits perturbations, the disjoining pressure $P_d \sim A_{132}/h_{\mathrm{min}}^3 \sim \mathcal{O}(10^0)$ Pa, considering the minimum film height of $h_{\mathrm{min}} \approx 200$ nm at the flat film region. Therefore, the inertial pressure dominates over capillary and disjoining pressure which leads to a gas pressure of $P_g \sim P_l \sim \mathcal{O}(10^2)$ Pa within the air film. After the droplet-air interface exhibits perturbations, the disjoining pressure $P_d \sim A_{132}/H_{\min}^3 \sim \mathcal{O}(10^2)$ Pa, considering the minimum film height of $h_{\min} \approx 50$ nm at the dimple region. Therefore, the gas pressure in the dimple region after perturbation follows $P_g \sim P_l + P_d \sim \mathcal{O}(10^2)$ Pa. The pressure gradient in the air film is sufficient to create a gas flow velocity of $\mathcal{O}(10^{-1})$ mm/s which is consistent with the experimentally measured values reported in Lo *et al.* [24] (see Fig. 3 in Ref. [24]). We speculate that either the shear flow at the drop-air interface or the interaction between the air cavity and the dimple top could be the source of the perturbations ultimately causing the dimple mode of contact.

IV. CONCLUSION

In conclusion, using theory and experiments, we showed that low-viscosity liquid drops impacting a smooth surface at We ≈ 4 exhibited a dimple mode of contact due to a combined effect of capillary wave and thin film instability. Experimentally measured capillary wavelength agreed well with theoretical studies [19,20]. The effects of increase in drop viscosity on suppression of the capillary wave and air cavity were found to be due to viscous dissipation attributed to the attenuation coefficient, α [21]. Interstitial air film profiles visualized using TIRM provided clear evidence of a thin film instability of the drop-air interface which occurred beyond the inertial-capillary timescale τ. Based on the thin film stability analysis [11], a critical wavelength $\lambda_{\max}^{\text{crit}}$ was obtained as a function of the minimum air film height $H_{\min}$. A good agreement was found between the experimental thin film perturbation wavelength $\lambda_{\exp}$ and $\lambda_{\max}^{\text{crit}}$, with $\lambda_{\exp} < \lambda_{\max}^{\text{crit}}$ for stable and $\lambda_{\exp} > \lambda_{\max}^{\text{crit}}$ for unstable films. We found that the absence of capillary waves over the drop surface and the thin film instability in the air film led to bouncing of higher viscosity on atomically smooth surfaces, consistent with previous bouncing studies [4,5]. A drop impacting a smooth surface at We < 10 could skate on a thin layer of air and eventually bounce, provided the drop viscosity is high enough to decay the capillary waves occurring over the drop surface. Finally, we showed that the presence of capillary waves and air cavity were the precursors for a thin film instability resulting in the dimple mode of contact.

ACKNOWLEDGMENTS

Support for this work was provided by the US National Science Foundation under Grant No. CBET-1705745. The authors thank Prof. Min Pack of Baylor University and Prof. Han Hu of University of Arkansas for the fruitful discussions.

[1] A. L. Yarin, Drop impact dynamics: Splashing, spreading, receding, bouncing …, Annu. Rev. Fluid Mech. **38**, 159 (2006).

[2] C. Josserand and S. T. Thoroddsen, Drop impact on a solid surface, Annu. Rev. Fluid Mech. **48**, 365 (2016).

[3] D. Richard and D. Quéré, Bouncing water drops, Europhys. Lett. **50**, 769 (2000).

[4] J. M. Kolinski, S. M. Rubinstein, S. Mandre, M. P. Brenner, D. A. Weitz, and L. Mahadevan, Skating on a Film of Air: Drops Impacting on a Surface, Phys. Rev. Lett. **108**, 074503 (2012).

[5] J. De Ruiter, R. Lagraauw, D. Van Den Ende, and F. Mugele, Wettability-independent bouncing on flat surfaces mediated by thin air films, Nat. Phys. **11**, 48 (2015).

[6] M. Pasandideh-Fard, Y. M. Qiao, S. Chandra, and J. Mostaghimi, Capillary effects during droplet formation on the solid surface, Phys. Fluids **8**, 650 (1995).

[7] R. Rioboo, C. Tropea, and M. Marengo, Outcomes from a drop impact on solid surfaces, Atomization Sprays **11**, 155 (2001) .

[8] L. Xu, W. W. Zhang, and S. R. Nagel, Drop Splashing on a Dry Smooth Surface, Phys. Rev. Lett. **94**, 184505 (2005).

[9] S. Mandre, M. Mani, and M. P. Brenner, Precursors to Splashing of Liquid Droplets on a Solid Surface, Phys. Rev. Lett. **102**, 134502 (2009).

[10] M. Mani, S. Mandre, and M. P. Brenner, Events before droplet splashing on a solid surface, J. Fluid Mech. **647**, 163 (2010).

[11] M. V. Chubynsky, K. I. Belousov, D. A. Lockerby, and J. E. Sprittles, Bouncing off the Walls: The Influence of Gas-Kinetic and van der Waals Effects in Drop Impact, Phys. Rev. Lett. **124**, 084501 (2020).

[12] J. de Ruiter, D. van den Ende, and F. Mugele, Air cushioning in droplet impact. II. Experimental characterization of the air film evolution, Phys. Fluids **27**, 012105 (2015).

[13] E. Q. Li, I. U. Vakarelski, and S. T. Thoroddsen, Probing the nanoscale: The first contact of an impacting drop, J. Fluid Mech. **785**, R2 (2015).

[14] K. R. Langley and S. T. Thoroddsen, Gliding on a layer of air: Impact of a large-viscosity drop on a liquid film, J. Fluid Mech. **878**, R2 (2019).

[15] M. Pack, H. Hu, D. Kim, Z. Zheng, H. A. Stone, and Y. Sun, Failure mechanisms of air entrainment in drop impact on lubricated surfaces, Soft Matter **13**, 2402 (2017).

[16] W. Bouwhuis, R. C. A. Van Der Veen, T. Tran, D. L. Keij, K. G. Winkels, I. R. Peters, D. Van Der Meer, C. Sun, J. H. Snoeijer, and D. Lohse, Maximal Air Bubble Entrainment at Liquid-Drop Impact, Phys. Rev. Lett. **109**, 264501 (2012).

[17] R. C. A. Van Der Veen, T. Tran, D. Lohse, and C. Sun, Direct measurements of air layer profiles under impacting droplets using high-speed color interferometry, Phys. Rev. E - Stat. Nonlinear, Soft Matter Phys. **85**, 264501 (2012).

[18] E. Klaseboer, R. Manica, and D. Y. C. Chan, Universal Behavior of the Initial Stage of Drop Impact, Phys. Rev. Lett. **113**, 194501 (2014).

[19] Y. Renardy, S. Popinet, L. Duchemin, M. Renardy, S. Zaleski, C. Josserand, M. A. Drumright-Clarke, D. Richard, C. Clanet, and D. Quéré, Pyramidal and toroidal water drops after impact on a solid surface, J. Fluid Mech. **484**, 69 (2003).

[20] D. Bartolo, C. Josserand, and D. Bonn, Singular Jets and Bubbles in Drop Impact, Phys. Rev. Lett. **96**, 124501 (2006).

[21] F. Behroozi, Fluid viscosity and the attenuation of surface waves: A derivation based on conservation of energy, Eur. J. Phys. **25**, 115 (2004).

[22] S. Lin, B. Zhao, S. Zou, J. Guo, Z. Wei, and L. Chen, Impact of viscous droplets on different wettable surfaces: Impact phenomena, the maximum spreading factor, spreading time and post-impact oscillation, J. Colloid Interface Sci. **516**, 86 (2018).

[23] M. Shirota, M. A. J. van Limbeek, D. Lohse, and C. Sun, Measuring thin films using quantitative frustrated total internal reflection (FTIR), Eur. Phys. J. E **40**, 54 (2017).

[24] H. Y. Lo, Y. Liu, and L. Xu, Mechanism of Contact between a Droplet and an Atomically Smooth Substrate, Phys. Rev. X **7**, 021036 (2017).

[25] J. M. Kolinski, L. Mahadevan, and S. M. Rubinstein, Drops can bounce from perfectly hydrophilic surfaces, Europhys. Lett. **108**, 24001 (2014).

[26] X. Tang, A. Saha, C. K. Law, and C. Sun, Nonmonotonic Response of drop impacting on liquid film: Mechanism and scaling, Soft Matter **12**, 4521 (2016).

[27] *Glycerine Producers' Association, Physical Properties of Glycerine and Its Solutions* (Glycerine Producers Association, New York, 1963).

[28] Clearco Products Co., PSF - 100,000cSt Pure Silicone Fluid Product Information, http://www.clearcoproducts.com/pdf/high-viscosity/NP-PSF-100,000cSt.pdf.

[29] J. de Ruiter, J. M. Oh, D. Van Den Ende, and F. Mugele, Dynamics of Collapse of Air Films in Drop Impact, Phys. Rev. Lett. **108**, 074505 (2012).

[30] See Supplemental Material at http://link.aps.org/supplemental/10.1103/PhysRevFluids.6.044002 for videos of drop shape and air film evolution of 1, 3 and 10-cP liquid drops impact.

[31] J. N. Israelachvili, *Intermolecular and Surface Forces*, 3rd ed. (Academic Press, Santa Barbara, CA, 2011).

[32] S. T. Thoroddsen, T. G. Etoh, K. Takehara, N. Ootsuka, and Y. Hatsuki, The air bubble entrapped under a drop impacting on a solid surface, J. Fluid Mech. **545**, 203 (2005).

[33] J. S. Lee, B. M. Weon, J. H. Je, and K. Fezzaa, How Does an Air Film Evolve into a Bubble during Drop Impact? Phys. Rev. Lett. **109**, 204501 (2012).

[34] S. T. Thoroddsen, K. Takehara, and T. G. Etoh, Dewetting at the center of a drop impact, Mod. Phys. Lett. B **23**, 361 (2009).

[35] L. Duchemin and C. Josserand, Rarefied gas correction for the bubble entrapment singularity in drop impacts, C. R. Mech. **340**, 797 (2012).